



## OPEN ACCESS

EDITED BY  
Natrayan L.,  
Saveetha University, India

REVIEWED BY  
Wenming Jiang,  
Huazhong University of Science and  
Technology, China  
Suryanarayanan R.,  
Vellore Institute of Technology (VIT),  
India

\*CORRESPONDENCE  
Essam B. Moustafa,  
✉ [abmostafa@kau.edu.sa](mailto:abmostafa@kau.edu.sa)

SPECIALTY SECTION  
This article was submitted to Polymeric  
and Composite Materials,  
a section of the journal  
Frontiers in Materials

RECEIVED 16 November 2022  
ACCEPTED 07 December 2022  
PUBLISHED 16 December 2022

CITATION  
Alzahrani MA, Moustafa EB, Alsoruji G  
and Mosleh AO (2022), The influence of  
the modifying elements on the  
microstructure, mechanical, and  
deformation properties of  
aluminum alloys.  
*Front. Mater.* 9:1100566.  
doi: 10.3389/fmats.2022.1100566

COPYRIGHT  
© 2022 Alzahrani, Moustafa, Alsoruji and  
Mosleh. This is an open-access article  
distributed under the terms of the  
[Creative Commons Attribution License  
\(CC BY\)](https://creativecommons.org/licenses/by/4.0/). The use, distribution or  
reproduction in other forums is  
permitted, provided the original  
author(s) and the copyright owner(s) are  
credited and that the original  
publication in this journal is cited, in  
accordance with accepted academic  
practice. No use, distribution or  
reproduction is permitted which does  
not comply with these terms.

# The influence of the modifying elements on the microstructure, mechanical, and deformation properties of aluminum alloys

Mahmoud A. Alzahrani<sup>1</sup>, Essam B. Moustafa<sup>1\*</sup>, Ghazi Alsoruji<sup>1</sup>  
and Ahmed O. Mosleh<sup>2</sup>

<sup>1</sup>Mechanical Engineering Department, Faculty of Engineering, King Abdulaziz University, Jeddah, Saudi Arabia, <sup>2</sup>Mechanical Engineering Department, Faculty of Engineering at Shoubra, Benha university, Cairo, Egypt

In the current work, the standard A242 aluminum cast alloy is modified using the stir casting method with titanium (Ti) (0.5% wt.) and boron (B) (0.1% wt.) modifiers. Polarized optical and scanning electron microscopy were utilized to examine the A242 base microstructure, and A242 + TiB modified alloys; the results revealed that the modified A242 + TiB alloy was refined by 13.5 times more than the as-cast alloy. The mechanical properties were investigated experimentally using compression test in addition to the hardness test; the results revealed that the ultimate compressive strength of the A242 + TiB modified alloy was increased by 9.0% more than those of the A242 standard alloy. Moreover, the yield stress was enhanced by 40% at room temperature and 20% at 250 °C. The dynamic properties were studied using a free vibration impact test to study the modifiers' effect on the dynamic behavior. The grain refinement notably impacted the damping capacity; due to the as-cast inhomogeneity, the conventional alloy A242 exhibited a greater FRF than the modified alloy A242 + TiB. The modified alloy displayed fewer resonance peaks due to grain refinement and excellent intermetallic phase distribution. The simulation process of the investigated alloys was performed using ABAQUS finite element software to predict the deformation behavior under different temperatures. The FE results showed that the modified alloy was more resistant to deformation by 9.1% than the reference alloy, A242, at room temperature and 7.6% at 250 °C, which agreed with the experimental findings.

## KEYWORDS

A242 alloy, industrial development, finite element, Ti-B modifiers, mechanical properties

## Introduction

Grain refining improves the completed or semifinished castings by uniformizing the microstructure. Refined grain structure during solidification reduces casting faults such as hot tearing and isolated porosity that reduce pressure tightness. A refined as-cast grain size may reduce homogenization times and improve recrystallized microstructures and

mechanical properties. Grain refining of Al-based alloys has been extensively researched over the past century, and both knowledge and technology have evolved (Murty et al., 2002). Today, grain refiners are directly lauded as master alloys. Most wrought Al-based alloys have aluminum-based master alloys with regulated quantities of titanium and boron, usually 3%–5% and 0%–1%, respectively. Al-Si foundry alloys and alloys with alloying components that poison Ti-B-based grain refiners have specialized grain refiners (Easton et al., 2011). Grain refining reduces defects and improves the casting properties of aluminum alloys. Solidification involves the nucleation and growth of  $\alpha$ -Al, which determines the aluminum grain size. Grain refiners introduce large heterogeneous  $\alpha$ -Al nucleation sites into the melt of aluminum alloys (Sigworth and Kuhn, 2007). Components that promote constitutional supercooling can accelerate heterogeneous nucleation. Solvent components (or insoluble particles) can accumulate between  $\alpha$ -Al nuclei and restrict expansion (Mi, 2018). Grain refinement in the cast and wrought aluminum alloys has become increasingly important as aluminum consumption increases. The alloys have coarse grains and are non-uniform in the as-cast state; the mechanical properties of sheet metal products are affected, i.e., the formability, yield strength, and tensile elongation are reduced (Kashyap and Chandrashekar, 2001). A coarse microstructure can cause surface defects in rolled or extruded alloys (Nie et al., 2020). Equiaxed microstructures allow rapid casting before hot fracture. The advantages of grain refinement include homogeneous distribution of second phases, fine microporosity, stronger feeding to minimize shrinkage porosity, and improved strength and fatigue life (Reddy et al., 2005). An improved lamellar or fibrous eutectic structure forms when elements such as titanium, boron, calcium, sodium, strontium, etc., are added to hypoeutectic aluminum alloys (Li et al., 2013; Chen et al., 2016; Moustafa and Mosleh, 2020). Scandium (Sc) is one of the most efficient aluminum alloying elements currently known (Chen et al., 2019). Modifying the  $\alpha$ -dendritic Al structure and limiting segregation can improve the mechanical properties of aluminum alloys. Sc affects the second phase of cast aluminum alloys (Wu et al., 2019). Adding 0.3 wt% Sc to Al-Mg changed the microstructure and refined the grains (Ren et al., 2021). Sc also reduced the subgrain size of Al-6Ni (Suwanprecha et al., 2018), although less significantly. When zirconium (Zr) replaces scandium (Sc) in  $\text{Al}_3(\text{Sc}_{1-x}\text{Zr}_x)$ , second-phase strengthening is improved (Harada and Dunand, 2002). Modifying the  $\text{Al}_3\text{Fe}$  main phase resulted in needle-like, granular, and flower-like structures. Sc and Zr atoms in the matrix were found to modify the material, but further research is needed to identify the enhancement law and the mechanism of action on the primary and eutectic phases in eutectic or hypereutectic cast aluminum alloys (Dai et al., 2022).

Grain size is reduced by combining a rapid nucleation rate with a grain expansion limitation. The carbide-boride theory, the peritectic theory, the duplex nucleation mechanism, and the

solute theory illustrate grain refinement by grain refiners. It was critical to determine if the grain refiner provided enough efficient nucleation sites to cause heterogeneous nucleation when applied to the aluminum alloys melt metal. Constitutional undercooling and heterogeneous nucleation sites are created by the elements Ti, V, Zr, and Nb, according to (Wang et al., 2014). Mondal et al. (Mondal et al., 2011) demonstrated that the high melting temperatures of intermetallic phases containing calcium, such as  $\text{CaAl}_2$ , were potential nucleation sites. Adding Al-B leads to grain refinement of aluminum alloy, and the nucleation sites in the Al-B master alloy are  $\text{AlB}_2$  phases (Nafisi and Ghomashchi, 2007; Bolzoni et al., 2015).  $\text{Al}_3\text{Fe}$  phases in the Al-Fe master alloy polished pure Al grains; moreover, the Al-Fe master alloy increased the nucleation rate while limiting the growth of  $\alpha$ -Al grains (Blunt et al., 2017). Insoluble particles (e.g.,  $\text{TiB}_2$ ) were not considered as  $\alpha$ -Al nucleation sites (Murty et al., 2002). The Al-5Ti-1B master alloy, which includes the  $\text{Al}_3\text{Ti}$  intermetallic compound and  $\text{TiB}_2$  particles in an aluminum matrix, is the most used grain refiner for Al alloys. With a Ti: B<sub>2</sub> ratio of 2.2:1, the Al-5Ti-1B master alloy has 2.8% more Ti than is necessary. A nucleation undercooling of less than 1 K makes the Al-5Ti-1B master alloy a potent tool for the grain refinement of most Al alloys (Ma et al., 2013; Fan et al., 2015; Loginova et al., 2022). Al-5Ti-1B as a refiner is the most available, easy to get, more effective for refining, and sharper than the other refiner elements (Guan and Tie, 2017). The SiCp element was added to AA6082 for refining the grains; thus, the SiCnp improved the 6082-aluminum alloy's microstructure, reducing the as-cast grain size from 386.6  $\mu\text{m}$  to 268.5  $\mu\text{m}$ . Furthermore, the mechanical properties are improved (Zhu et al., 2020; Jiang et al., 2021). Effective modeling of aluminum sheet forming requires reliable finite element models (FE) that account for actual contact conditions. Consequently, tests performed to quantify mechanical properties are critical to developing contact models that accurately represent the mechanical behavior of the deformed sheets. The underlying microstructure and crystallographic texture determine the anisotropy of the aluminum structure during elastoplastic deformation; therefore, many crystal plasticity models are considered to have these properties (Lebensohn and Tomé, 1993; Anand, 2004; Knezevic et al., 2008; Zecevic et al., 2019). These models require the framework of FE to account for the geometric aspects of components during the forming process (Knezevic et al., 2013a; Knezevic et al., 2013b).

Whenever high strength and hardness are required, as is often the case in the industry, alloy 242 is a preferred material. Common applications include aircraft generator housings and heavy-duty pistons for motorcycles, diesel engines, and aircraft. Due to its low flowability and misrunning, it is unsuitable for complicated, heavy cross-sections (blocks/heads). The intermetallic compound  $\text{Al}_2\text{Cu}$  is created as a result of a eutectic reaction during the solidification of the 242-aluminum alloy, increasing resistance and hardness in the

as-cast condition. On the other hand, once nickel solidifies, it joins with aluminum to form the intermetallic  $Al_3Ni$ , which has better characteristics at high temperatures and a lower coefficient of thermal expansion. Therefore, in the current investigation, the standard alloy A242 is modified by adding modifiers to meet the requirements of industrial development processes. Thus, the Ti-B modifiers refine the grain structure of the standard alloy to improve its mechanical properties. The effect of grain refinement on dynamic properties is being studied; thus, the improvement of damping capability plays an important role in aerospace, submarine structures, and automotive parts. The main reason for choosing Ti-B as a refining element in the current work is its high effectiveness and low cost compared to the other refining elements. The study of the influence of grain refinement of metal granules on the forming processes is of great importance for the economy of the process. In addition, the aim of this work is also the prediction of stress and vulnerability during the deformation process using the FE software. The behavior of the studied alloys is successfully simulated using ABAQUS finite element software to predict the weak points and the maximum stress during the deformation process.

## Materials and methods

The chemical compositions of the A 242 aluminum alloy and the modified alloy with TiB are shown in Table 1. The casting process was carried out in a Nabertherm electrical resistance furnace at a temperature of  $800^{\circ}C \pm 20^{\circ}C$ . The molten metal was cast in a copper mold with inner dimensions of  $20 \times 40 \times 120$  mm and a casting cooling rate of 15 K/min. The components were thoroughly centrifuged throughout the casting process to blend all alloying ingredients together. For microstructure characterizations, the samples were cut from the as-cast ingots. The samples were ground using a grinding paper (SiC papers) starting from 120 to 4,000 grit in the water media as a lubricant. Then the samples were polished using emery papers in the alumina suspension with a diameter of  $0.1 \mu m$  as abrasives for polishing. The polished surfaces were cleaned and dried before the etching. The polished surfaces were electrochemically etched at 18 V with a 10% electrolyte (saturated solution of  $H_3BO_3$  in HF) in distilled water. This was performed by using optical microscopy (OM, Olympus BX51) and scanning electron microscopy (SEM, Philips XL30) to examine grain microstructures. The usual linear intercept approach was used to determine grain size.

For mechanical characterization, the compression test was performed using a universal testing machine Zwick/Roell Z250 Allround series testing machine (ZwickRoell GmbH & Co. KG, Ulm, Germany) according to the ASTM E9 standard with a strain rate of 4 mm/min and at room temperature and  $250^{\circ}C$ . Three compression samples were tested for each alloy, the average was

taken, and the data was presented. Vickers microhardness tests were conducted using a Zwick Roell microhardness tester (ZwickRoell GmbH & Co. KG, Ulm, Germany) in accordance with the ASTM E384-17, with a shutter speed of 10s and a load of 100 g. The hardness test was carried out after the samples had been cut, ground, and polished for microstructure examination. To ensure the reliability and confidence in hardness values, ten points at different places were measured, and the average was calculated for each alloy.

## Free vibration impact test

Figures 1A shows the schematic representation of the free vibration test. A specimen cantilever beam was subjected to dynamic testing. The frequency spectrum of each specimen was triggered by hitting the free end of the bottom side with a rubber tip hammer (Type 8206, Bruel & Kjaer) and received by a piezoelectric accelerometer (Type 4507-B, Bruel & Kjaer, Naerum, Denmark). A LAN-XI pulse analyzer was used to collect the vibration signals (type 3050 A-60, Bruel & Kjaer). The Pulse Lab Shop and MEscape (Vibrant Technology Inc. Scotts Valley, CA, United States) The software was used to process the signal after acquisition. The FFT was computed using a frequency range of 10 k Hz and a resolution of 3,200 lines. In a linear mode, ten data blocks were averaged together. All samples were analyzed using an average of five samples for each alloy. In order to calculate the damping ratio ( $\zeta$ ), the first resonant frequency ( $F_n$ ), and the dynamic modulus ( $E_d$ ), the following equations were used depending on the free vibration decay curves of a cantilever beam (Moustafa, 2018; Ahmed et al., 2021; Moustafa and Almitani, 2021).

$$\delta = \frac{1}{n} \ln \frac{x_o}{x_n} \quad (1)$$

$$\zeta = \frac{\delta}{\sqrt{4\pi^2 + \delta^2}} \quad (2)$$

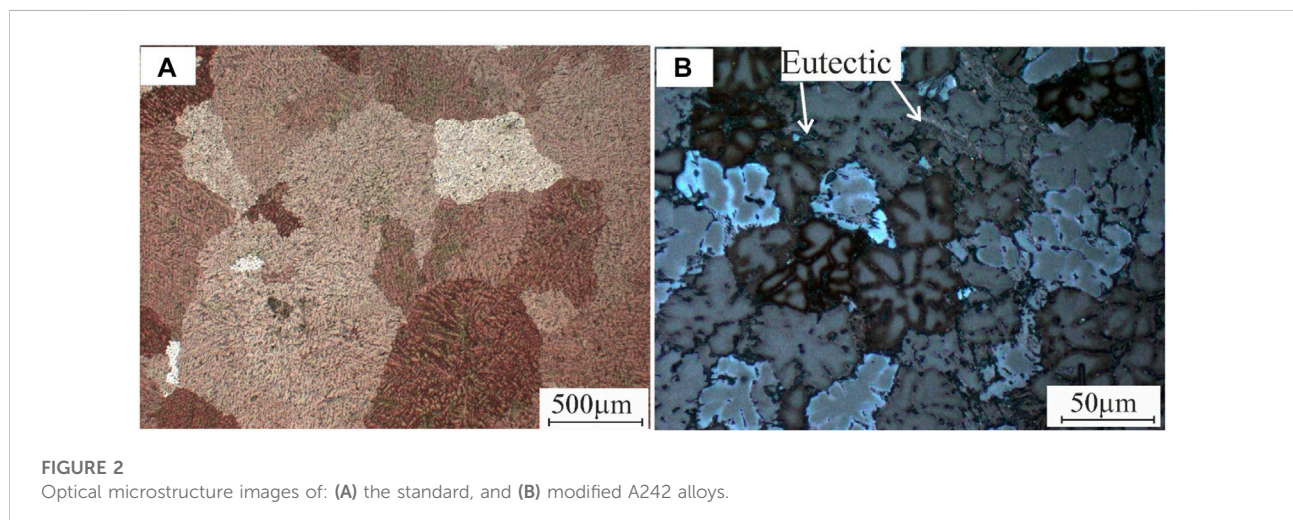
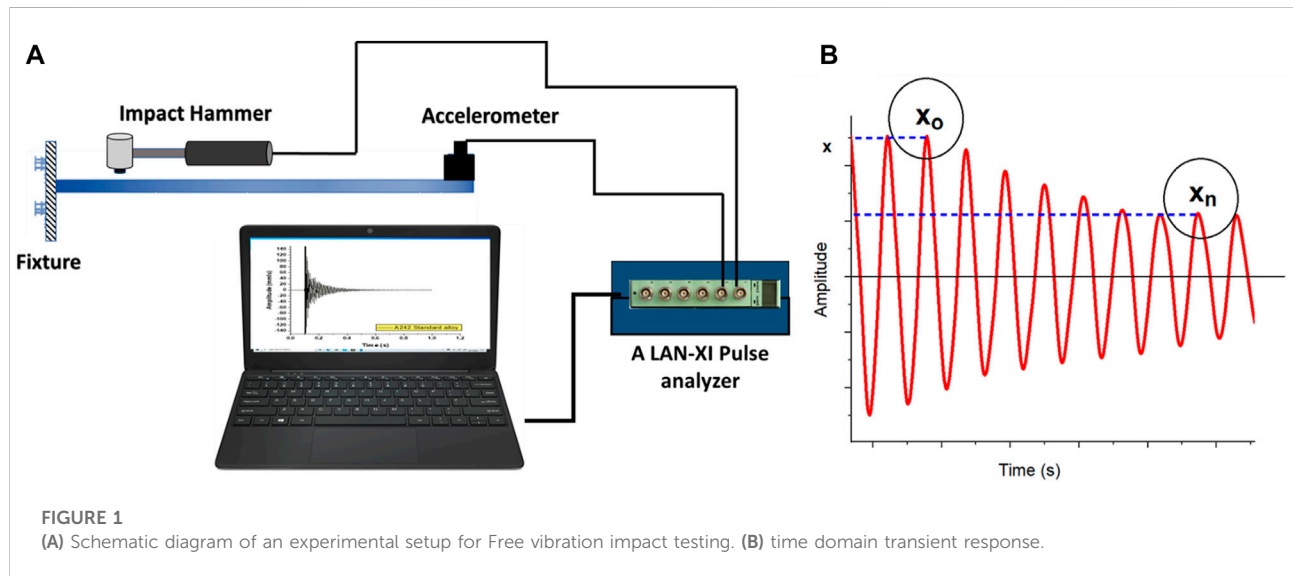
$$E_d = 16\pi^2 [M + (0.236)m] \frac{L^3 f_n^2}{wt^3} \quad (3)$$

$$E_{\text{loss modulus}} = E_d \times \eta \quad (4)$$

Where  $X_o$  and  $X_n$  are the amplitude located from the time domain at a number of cycle  $n$  as shown in Figures 1B.  $M$  is the mass of the accelerometer and mounting clips of  $6.0 \times 10^{-3}$  kg, the distributed mass of the cantilever beam  $m$  is  $10.0 \times 10^{-3}$  kg,  $L$  is the beam length (0.13 m),  $f_n$  is the first resonant frequency that determined from both method the logarithmic decrement curve calculations and the frequency response function (FRF),  $w$  (0.01 m) and  $t$  (0.003 m) are the width and thickness of the cantilever beam and  $\eta$  is the loss factor = complex loss modulus/storage modulus. The loss factor is obtained from the half bandwidth method from FRF curve (Hammad and Moustafa, 2020; Basha et al., 2022).

**TABLE 1** Chemical compositions of the standard and modified A 242 alloy.

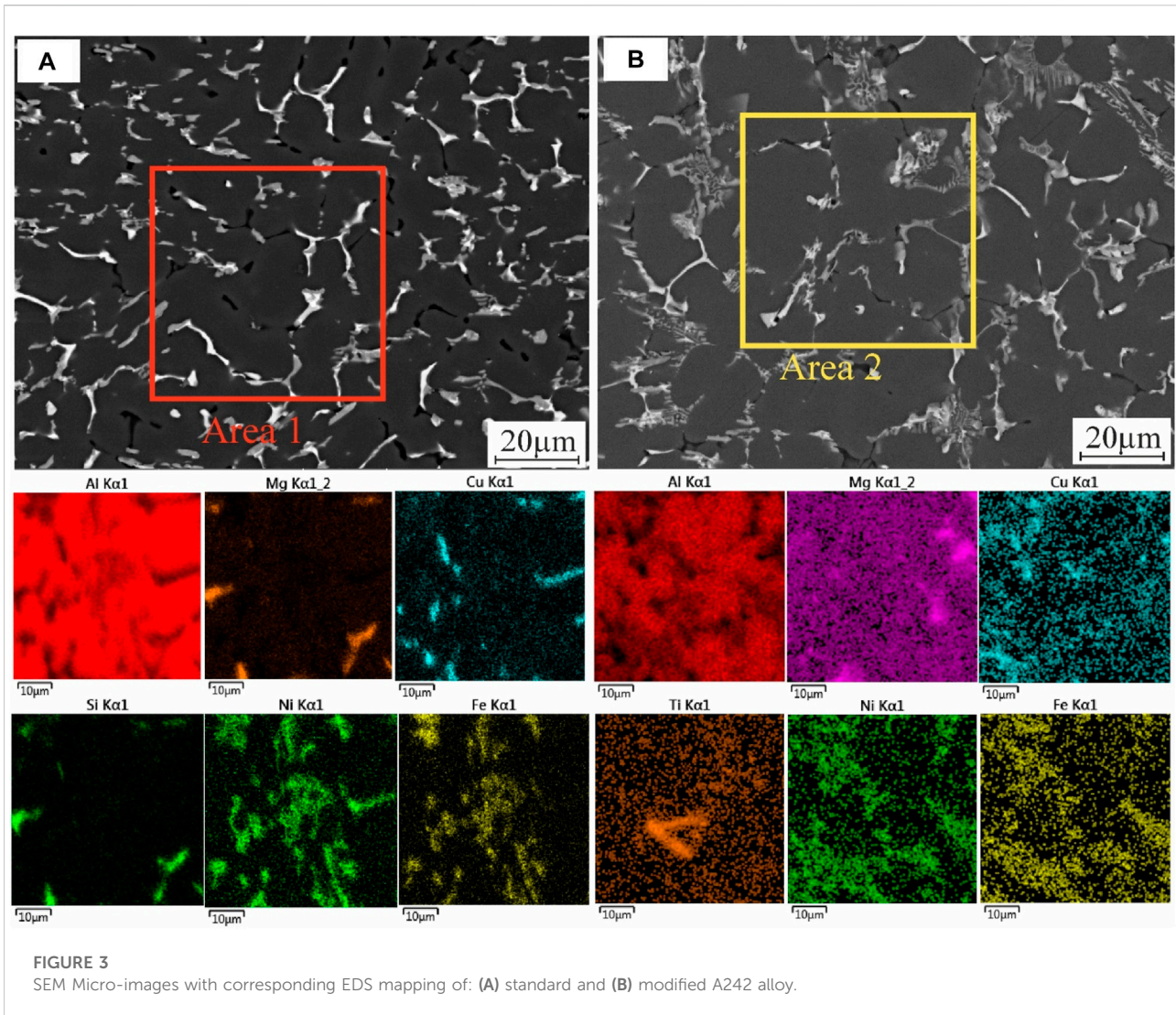
	Cu	Mg	Si	Zn	Fe	Ni	Mn	Cr	Ti	B
A 242	4.5	1.42	0.48	0.5	1.0	2.1	0.4	0.25		
A 242-TiB	4.46	1.38	0.38	0.55	1.06	2.1	0.45	0.3	0.5	0.1



## Microstructure observations

The nucleation and development of  $\alpha$ -Al during solidification determine the grain size of the aluminum alloy. It has been shown that boron, when combined with an excess of titanium, is more efficient than boron alone (at values of 0.005%–

0.1%) in the role of grain refiner during solidification. In commercial grain refineries, titanium and boron are often found in a 5-to-1 ratio. In this step, grain refiner is added to the aluminum alloy melt to create massive heterogeneous nucleation sites of  $\alpha$ -Al. Solution components that cause constitutional supercooling can also accelerate heterogeneous



nucleation. When  $\alpha$ -Al nuclei form, the solution components (or insoluble particles) can clump and hinder their development. As a result of the high nucleation rate and the constraints imposed on grain development, the grain size is reduced. Optical microstructure pictures of the standard A242 aluminum alloy, as well as the modified A242 + TiB aluminum alloy, are shown in Figure 2. When TiB modifiers were added to the casting process, it resulted in a refinement of the grains, which led to an equiaxed refined dendritic structure. Without undergoing any extra processing, the improved A242 + TiB alloy displayed grains that were homogenous, equiaxed, and refined to be three times smaller than those of the standard alloy. The standard A242 alloy was analyzed using ImageJ software, and the average grain size was observed as  $470 \pm 80 \mu\text{m}$ , while the modified A242 + TiB has a  $35 \pm 5 \mu\text{m}$  average grain size. The A242 alloy, much like the reference alloy, had big grains and a typical coarse dendritic

structure. The grain size of the dendrites had a substantial impact on both the geometry of the dendrites and the structures that formed after solidification. Adding 0.50% titanium and 0.10% boron to alloy A242 modified the material's grain shape and phase structure. These modifications included the transformation of coarse dendrites into homogenous and refined primary  $\alpha$ -Al grains.

Scanning electron microscopy (SEM) was employed to analyze the chemical composition and the formed phase in the investigated alloys. Figure 3 shows the SEM micrographs and the EDS maps for different elements for reference and modified alloys. The EDS maps confirm the uniform distribution of the interdimeric phases along the dendritic arms. For the modified alloy with Ti-B, the Ti element appeared due to its suitable weight percentage in the alloy, while the B element did not appear due to its lower percentage

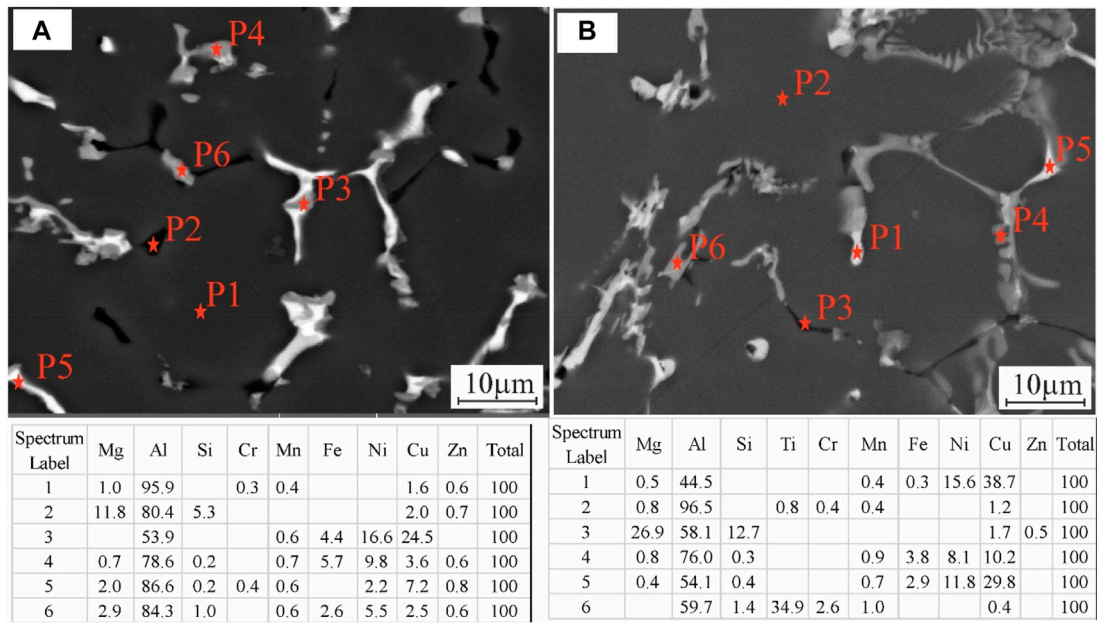


FIGURE 4 SEM Micro-images with corresponding EDS point analysis of: (A) standard and (B) modified A242 alloy.

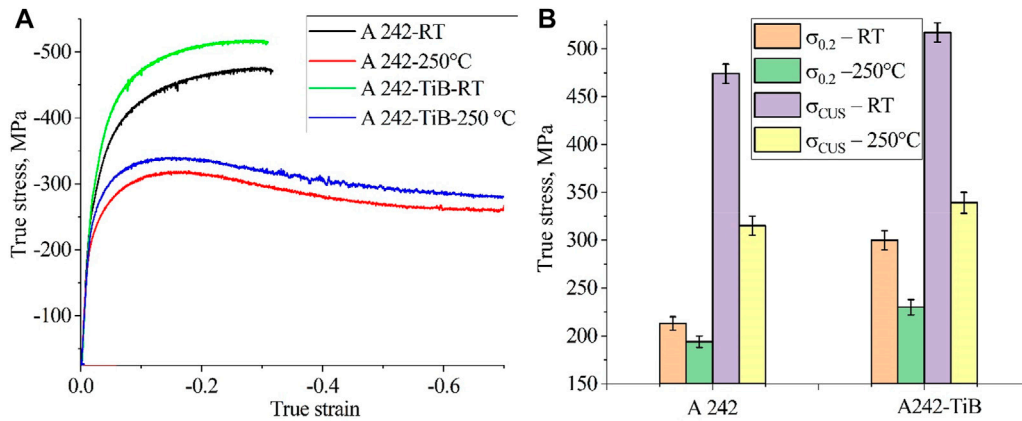
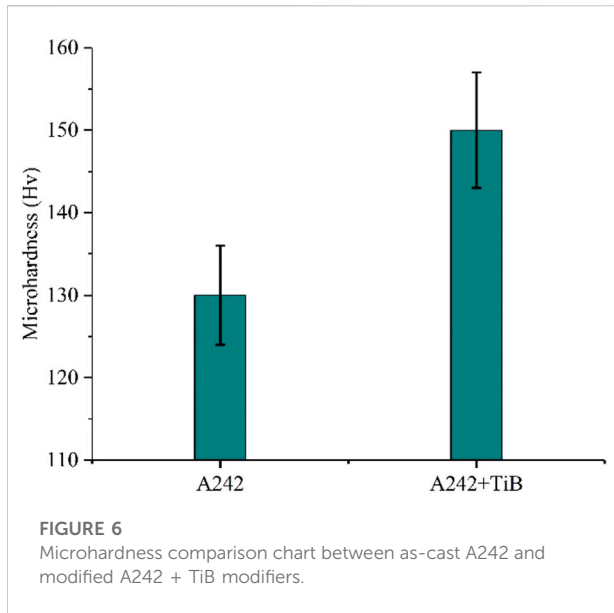


FIGURE 5 Mechanical properties, (A) Stress-strain diagram, (B) Ultimate compression stress.

TABLE 2 Quality index of the investigated alloys.

Sample	Quality index (QI)
Standard A242	203.65
Modified A242 + TiB	236.48

of 0.1% and its light atomic weight, as shown in Figure 1C, D. Figure 4 shows the EDS point for the formed phases in the standard and modified alloys. The EDS analysis confirms the presence of the metallic phases of  $Al_2Cu$ ,  $Mg_2Si$ ,  $Al_3Ni$ , and  $Al_9FeNi$  based on the  $\alpha$ -Al solid solution in the reference alloy. These results are in agreement with (Rodríguez et al., 2012).

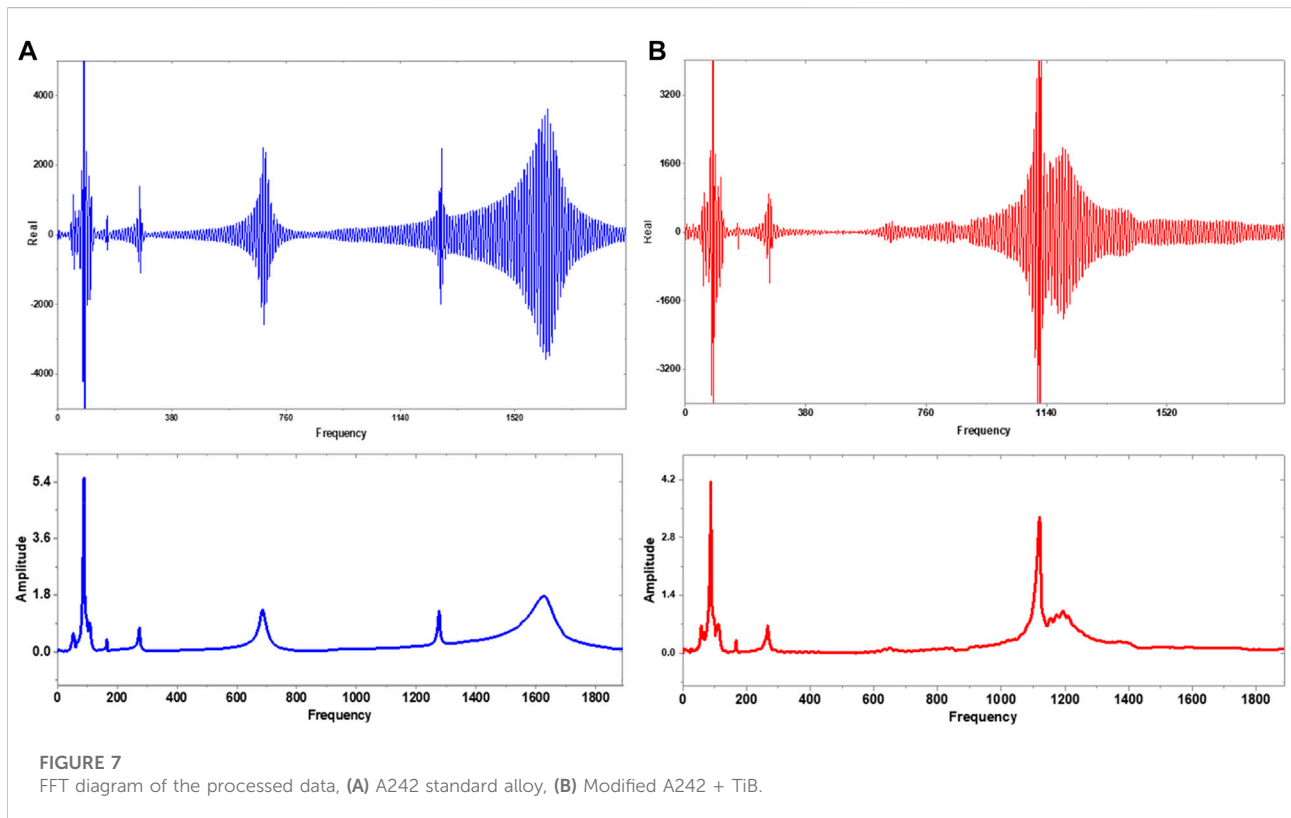


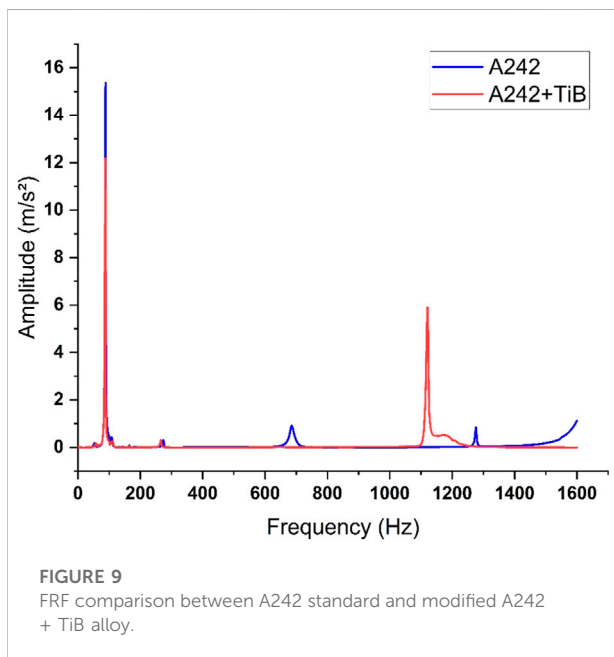
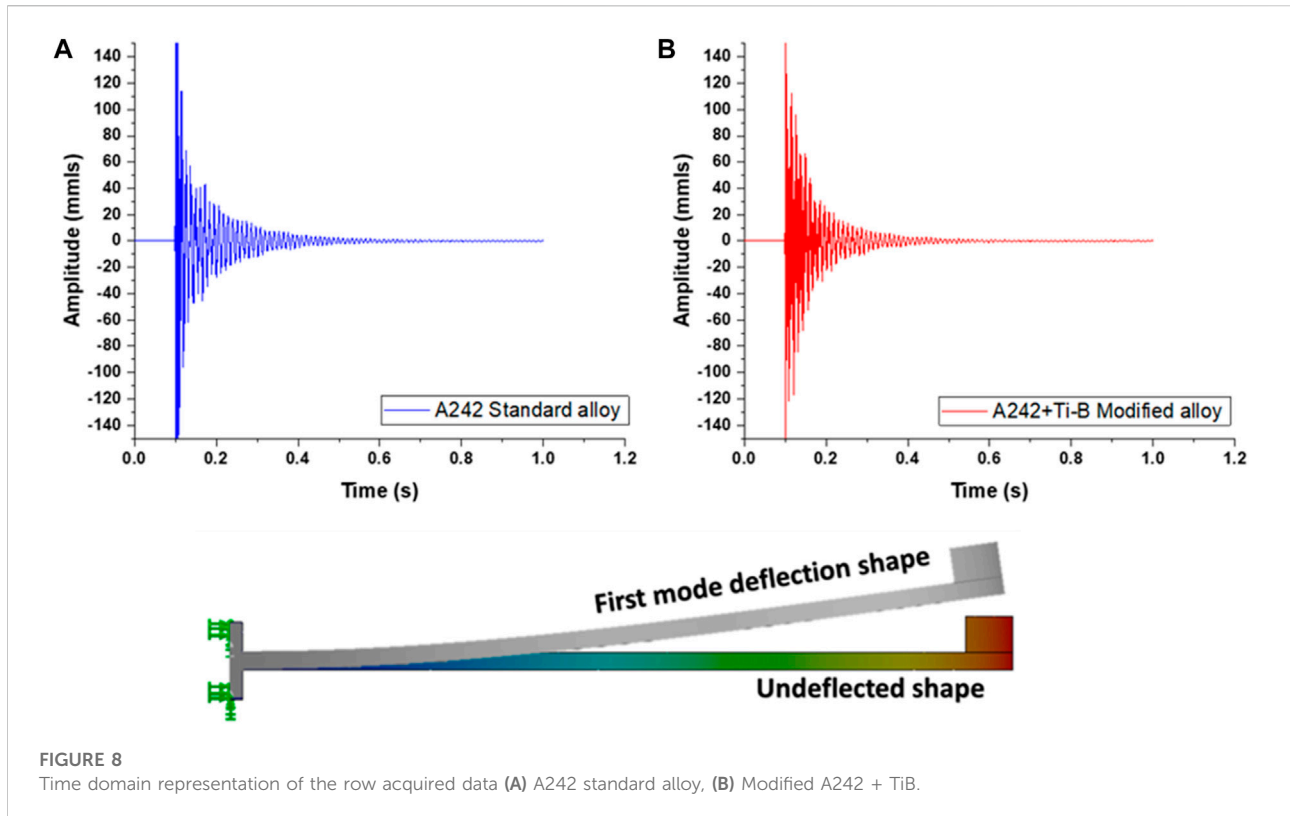
For the modified alloy, the presence of Ti-B resulted in an equiaxed dendritic structure surrounded by the eutectic phases (Figures 2B, 3B, 4B). The main reason for the refinement of the dendritic structure is the presence of the heterogeneous nucleation centers  $TiB_2$  and  $Al_3Ti$  which in agreement with (Mosleh et al., 2021).

## Mechanical properties

Figure 5 presents a comparison of the compression strength and elongation findings in tested samples; thus, the standard and modified A242 alloy were evaluated at both room temperature (RT) and 250°C. At room temperature, the compressive yield strength of ( $\sigma_{0.2}$ ) for the reference and the modified alloy was  $213 \pm 7$  MPa and  $300 \pm 10$  MPa, respectively. The improvement in the compressive yield in the modified alloy with Ti-B can be attributed to the refined structure, which increased the boundaries of the grains and acted as a barrier for the dislocation movements (Pattnaik et al., 2015). The ultimate compressive strength (CUS) value of the modified alloy reached 510 MPa at room temperature. These results are in agreement with (Kurt et al., 2015; Wang et al., 2021), which attributed to the refining effect of the TiB. As shown in Figures 13B, the CUS of this modified alloy had a greater value than that of the conventional A242 alloys used in manufacturing automobile component parts.

Compared with the other Al-Cu-Mg alloys, 242 alloys with 2% Ni and 1%Fe exhibit high compressive strength (Trejo Rivera et al., 2019). Due to iron's limited solubility in the solid state (0.04%), most of the iron contained in aluminum exceeds this proportion as an intermetallic second phase with aluminum and possibly other elements such as  $Al_3Ni$ ;



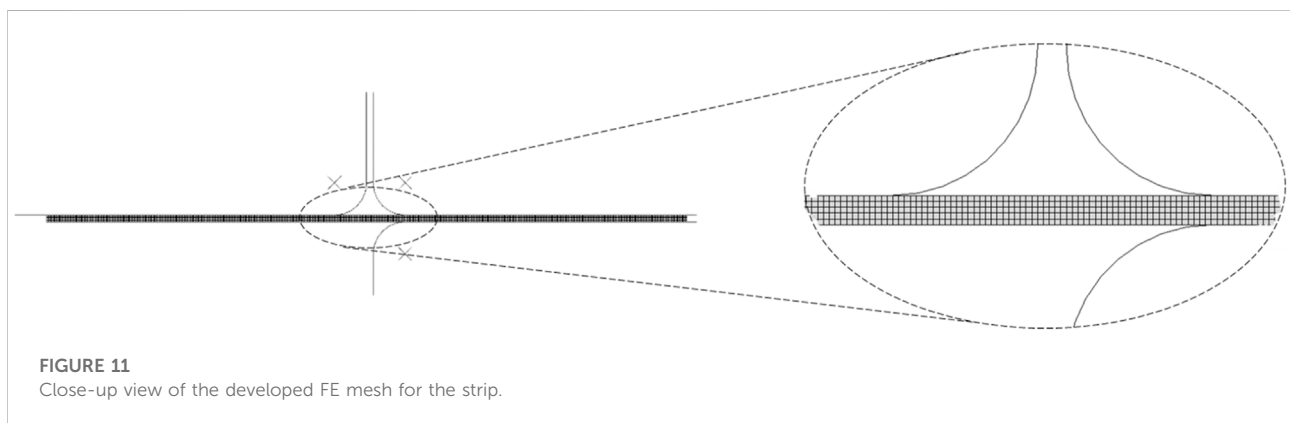
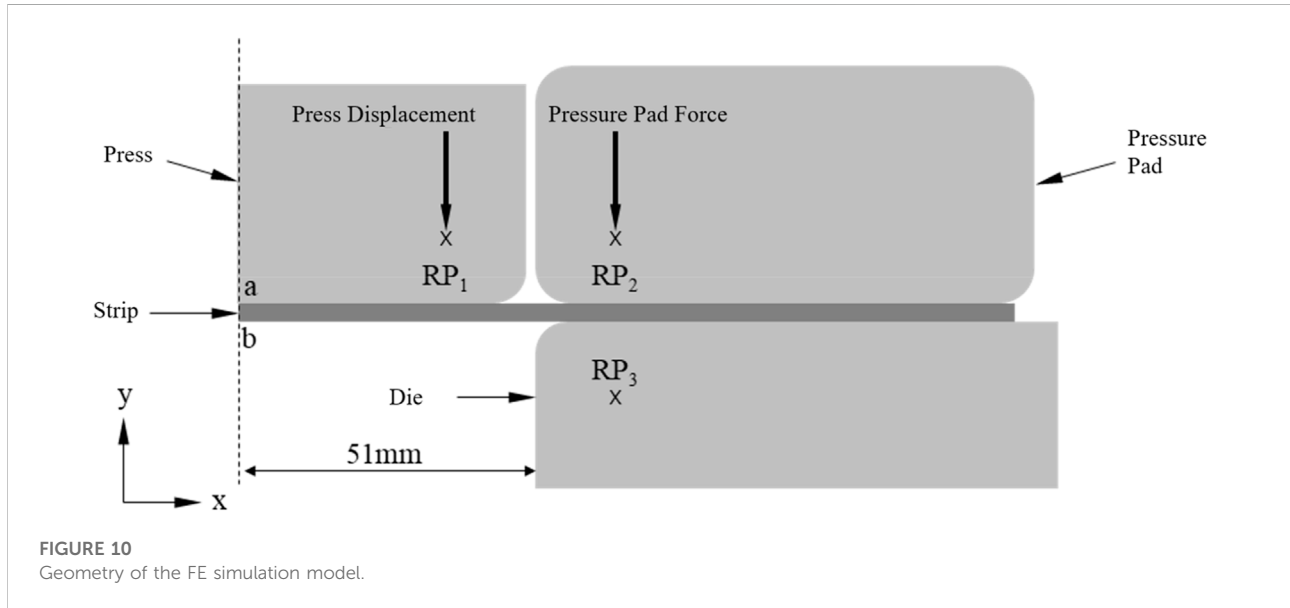


moreover, with 1.0% iron, the strength of the alloy is increased. Solid nickel is 0.04% soluble in aluminum; hence, the two elements seldom interact. At this point, it forms an insoluble intermetallic complex with iron as

$Al_9FeNi$ . Nickel boosts hardness and strength at high temperatures and minimizes expansion in A242 alloy. Due to the grain refinement and redistribution of the alloying elements in the modified A242 alloy, the CUS increased by 1.45 times that of the standard A242 alloy at room temperature. As mentioned in the introduction section, the 242 aluminum alloy is widely used in cylinder heads for motorcycles and pistons; thus, it is important to maintain the mechanical properties of this alloy at an acceptable level. In this context, the compressive test at 250°C was performed for both standard and modified alloys. Increasing the temperature, both compressive yield and ultimate strengths decreased (Gündüz and Acarer, 2006). Increasing the temperature facilitates the dislocation movements resulting in low characterizations. At 250°C, the  $\sigma_{0.2}$  and  $\sigma_{CUS}$  decreased to  $194 \pm 6$  MPa and  $315 \pm 10$  MPa, respectively. There is a direct correlation between refined granules and mechanical qualities; hence, the findings revealed that granule reduction enhanced the distribution and size of the alloying components and generated phases during the casting process, which is reflected in mechanical behavior. Effects of grain refiners on certain properties Alloy A242 It has been found that adding an appropriate number of grain refiners improves compressive yield and ultimate strengths compared with the reference alloy at 250°C. The most important explanation for this improvement is probably the smaller equiaxed dendrites'

**TABLE 3** Dynamic properties obtained from the free vibration test analysis.

Alloy	Static young's modulus $E_s$ (GPa)	Dynamic young's modulus $E_d$ (GPa)	Damping ratio $\zeta$ (%)	First resonant frequency $F_n$ (Hz)	Loss factor $\eta$	Loss modulus $E_{loss}$ (GPa)
A242	$71.21 \pm 0.48$	$71.06 \pm 0.11$	1.68	87.89	0.0340	2.41
A242 + TiB	$72.64 \pm 0.79$	$71.22 \pm 0.13$	1.81	88.99	0.0392	2.79



size, which leads to a finer distribution of the second phases (i.e., the intermetallic phases) surrounding the dendrites (Kobayashi, 2000). The grain refinement provides a more uniform distribution of elements in the microstructure by creating heterogeneous nucleation sites with  $Ti_2$  and  $Al_3Ti$  (Murty et al., 2002; Fan et al., 2015). In general, most

aluminum alloys' compressive yield points fall below 100 MPa as the temperature is raised above 250°C, while in the standard and modified alloys, the compressive yield strength was 194–230 MPa at 250°C. The quality index  $Q$  is represented by the equation Eq. 5 and is defined as a semilogarithmic plot of ultimate tensile strength *versus*

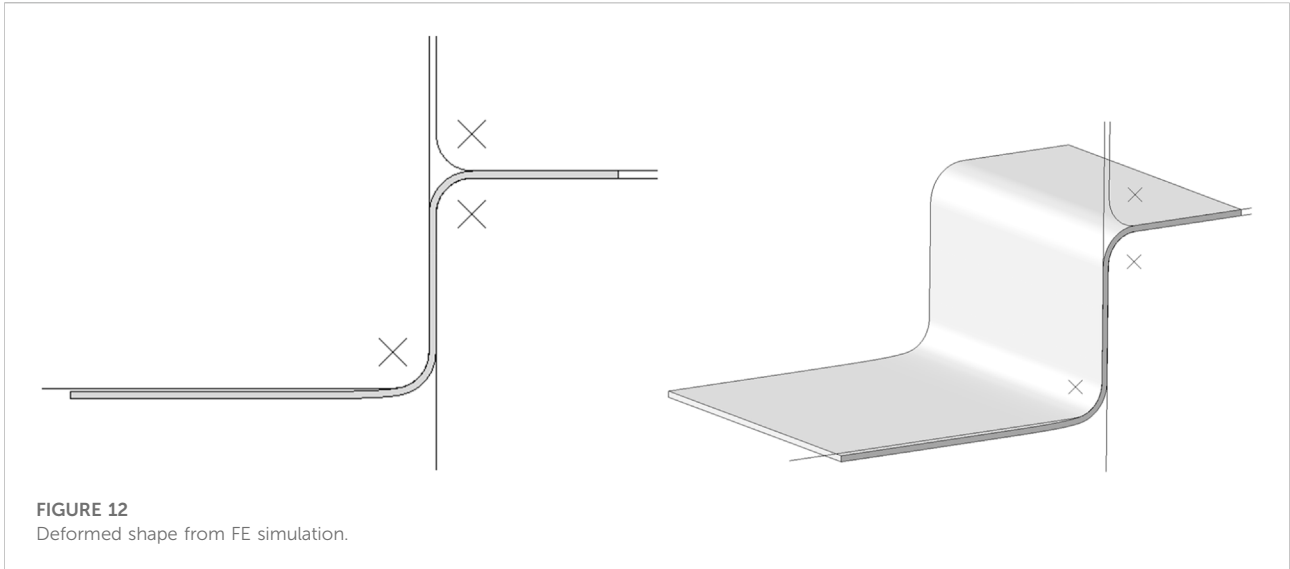


**FIGURE 12**  
Deformed shape from FE simulation.

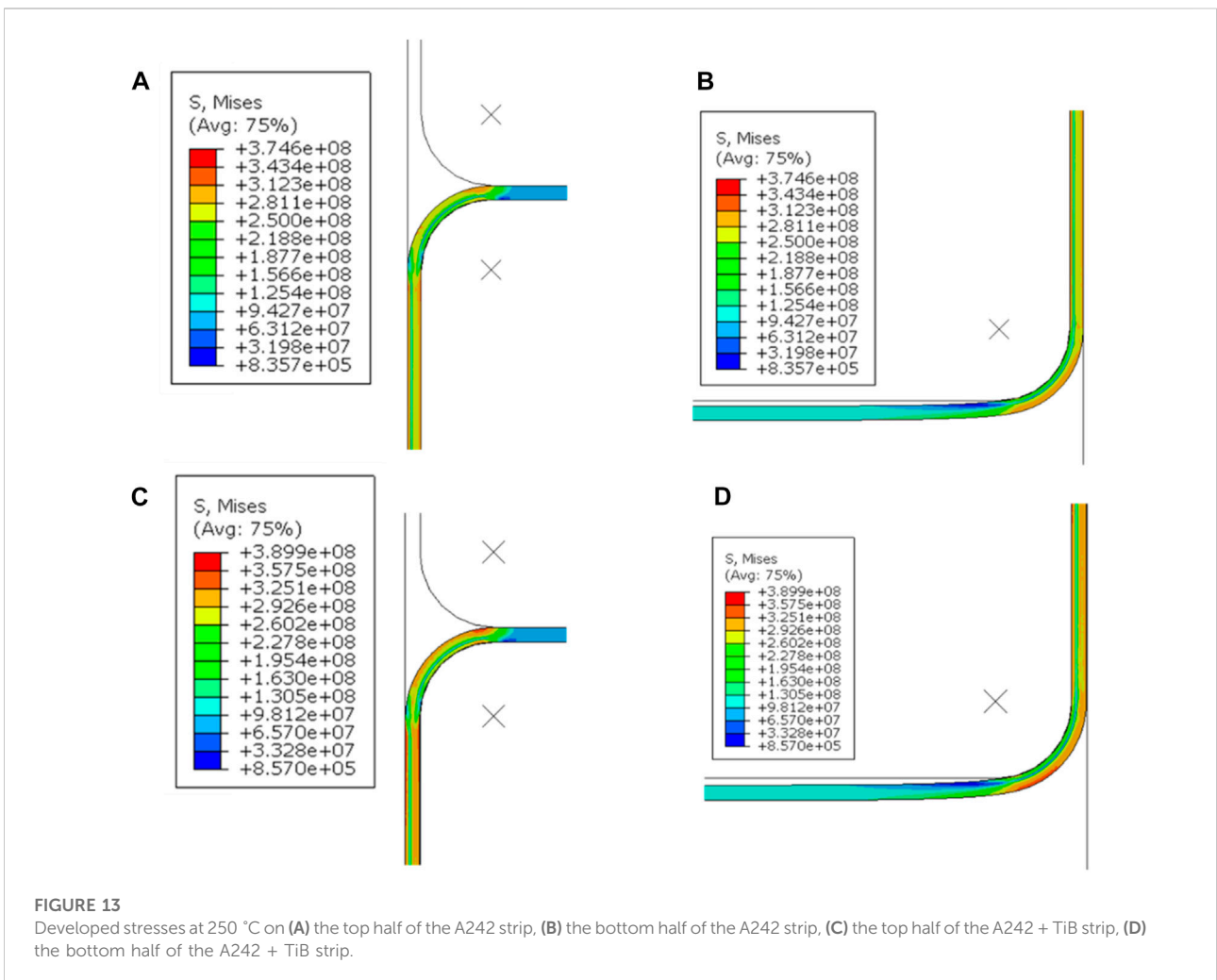
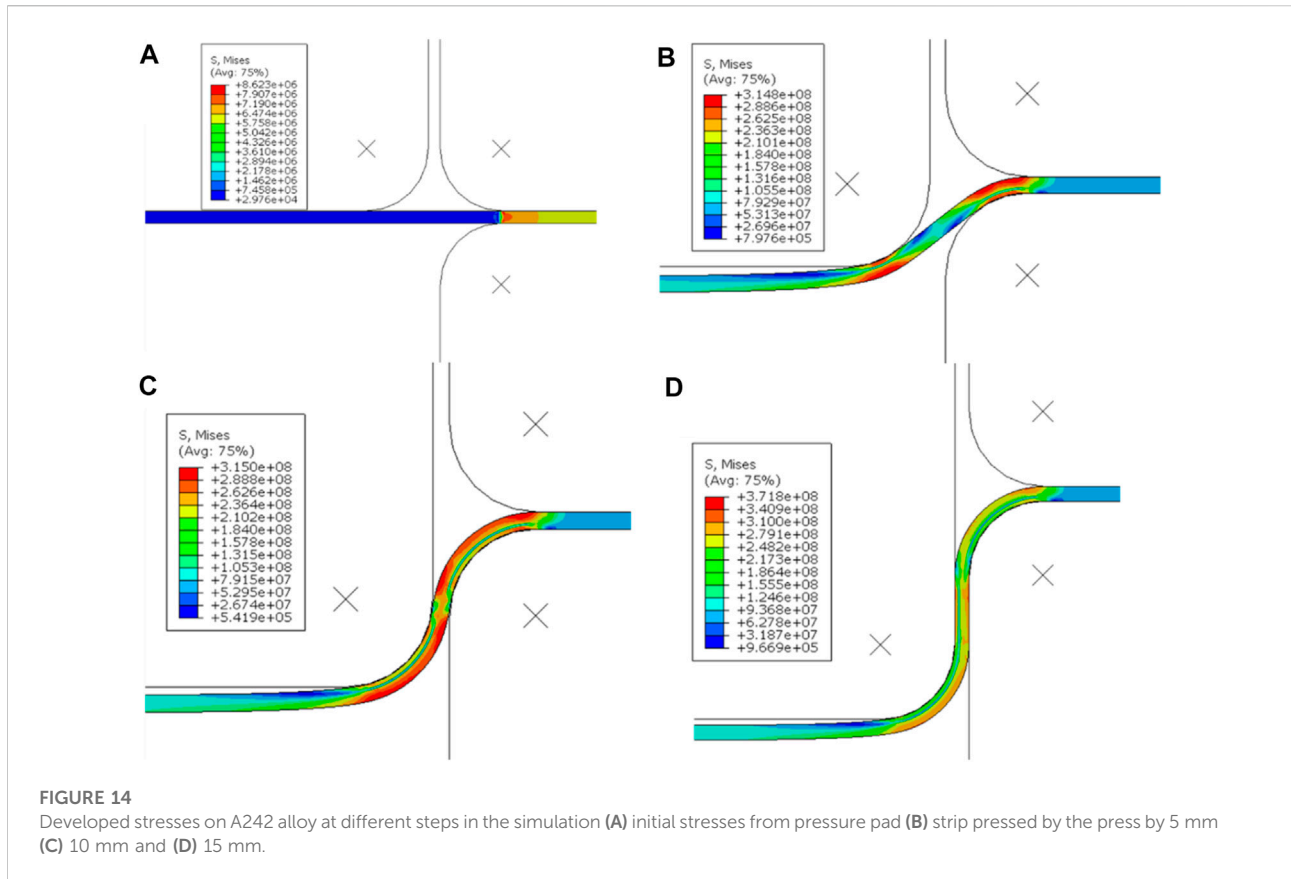


**FIGURE 13**  
Developed stresses at 250 °C on (A) the top half of the A242 strip, (B) the bottom half of the A242 strip, (C) the top half of the A242 + TiB strip, (D) the bottom half of the A242 + TiB strip.



elongation to fracture. (Wang et al., 2010; Khorshidi et al., 2011):

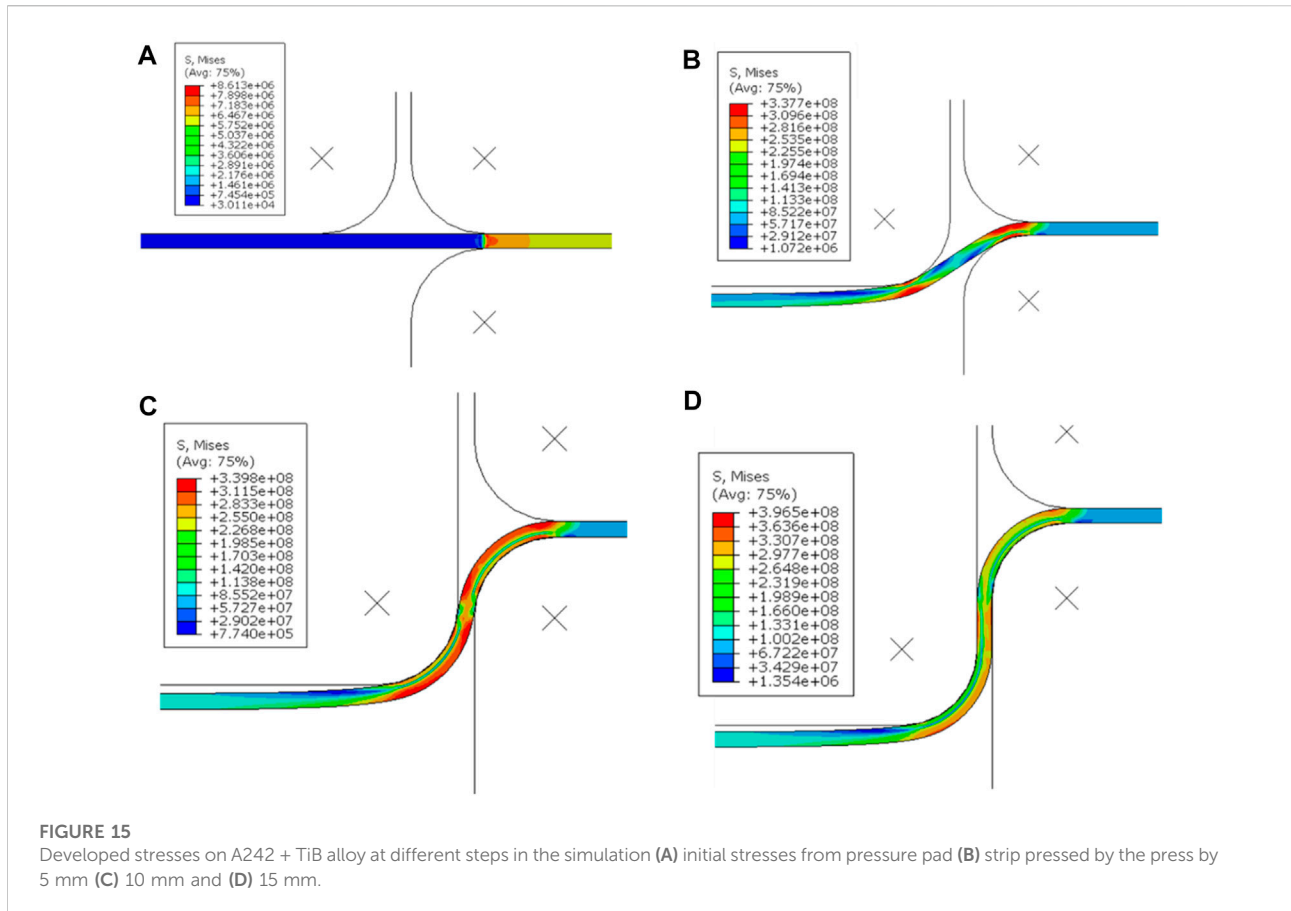
$$Q = UTS [MPa] + \text{Log} (\epsilon\%) \quad (5)$$

Table 2 shows the quality index for each alloy studied. It can be seen that the refined alloy Ti-B achieves the highest quality index. The main reason for this improvement is that the grain size of the castings has decreased, resulting in a more uniform distribution of the finer second phases. The microhardness values of the investigated alloys revealed that the TiB modifier elements have a significant effect on the improvement of the overall hardness. The modified alloy increased by 20 HV more than the as-cast alloy, as shown in Figure 6. The main reason for increasing the hardness can be attributed to the refining effect of the TiB and the uniform distribution of the second phases in the modified alloy.

## Dynamic properties

The study of dynamic properties is one of the most critical pillars used during the design stages of products that are exposed to high operational load and conditions. The

natural frequency and damping capacity are among the most important features that determine the dynamic behavior of materials. This study experimentally performs a free vibration impact test to identify the dynamic behavior. The time and frequency domains are used to analyze the acquired data, as shown in Figure 7; the real amplitude with corresponding Fast Fourier Transform FFT is represented for each sample. Figure 7A shows the as-cast A242 alloy acoustic behavior through different frequencies, while Figures 7B shows the modified A242 + TiB alloy. The vibration signals revealed that as-cast alloy excites more resonant frequencies in the frequency range between 80 and 1,200 Hz. In contrast, the modified A242 + TiB alloy absorbed the resonant frequency in the same range. The resonant frequencies at 680 and 1,269 Hz are observed only in standard A242 alloy; thus, they can be attributed to the random distribution of the intermetallic phases and extra-large grains during the solidification process. The absence of these resonant frequencies in the modified alloy means that the homogeneity of the modified A242 + TiB alloy is well-created. Through the use of the time domain curve, dynamic properties were able to be determined, as seen in Figure 8. Calculations are performed on the data using the initial



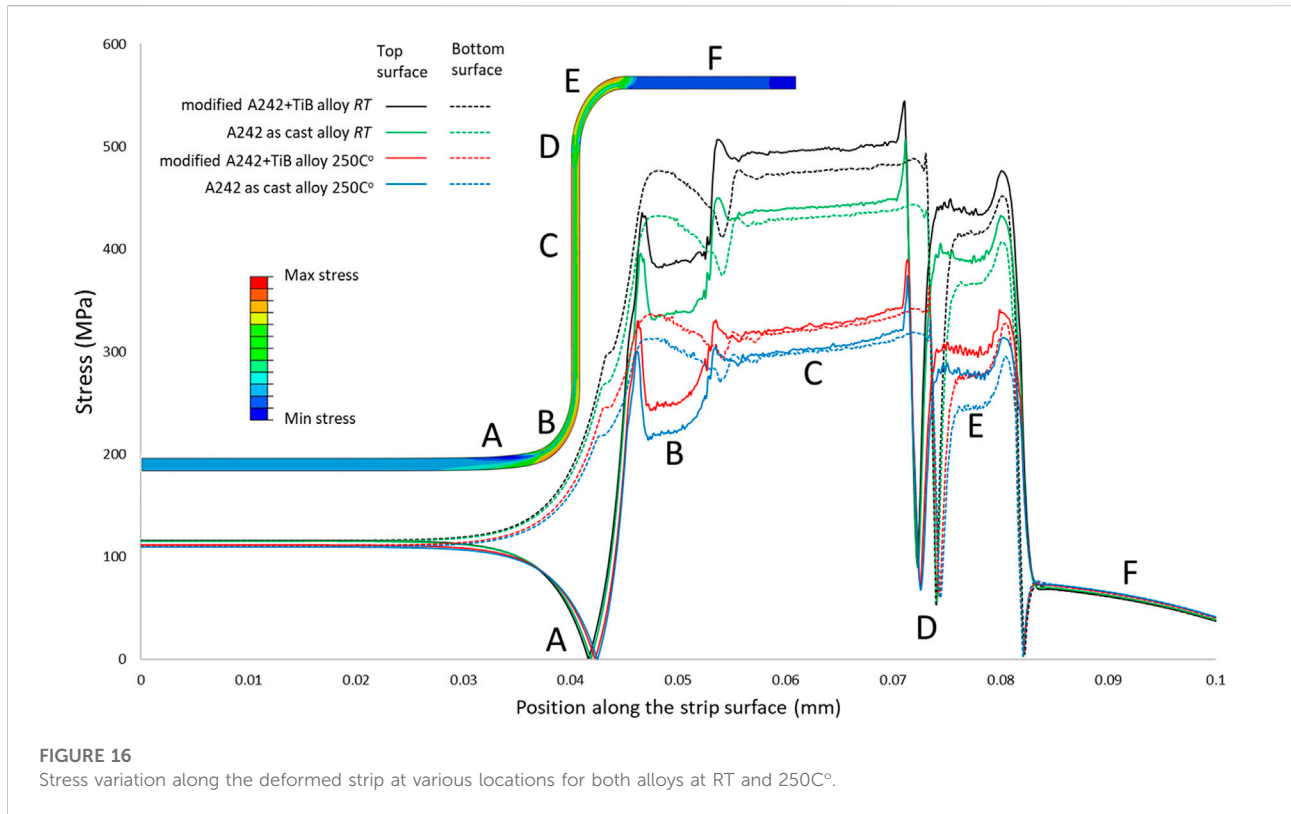
resonant frequency as the basis (first mode). In Figure 9, we see a comparison of the frequency response functions (FRFs) that were calculated using FFT analysis applied to the time domain for both of the studied alloys. The new resonance peaks developed in the 600–800 Hz region that corresponded to the standard alloy A242. This points to the fact that the structure of the coarse grain and the random production of the intermetallic phases create greater resonant frequencies in the cast than in the homogenized modified alloy. Table 3 provides a summary of the dynamic characteristics of the investigated alloys. The results revealed little change in the dynamic properties of the investigated samples; however, the damping ratio increased due to the refinement of the grain, which reflects the metal's responsiveness to the external effect of mechanical vibrations. Table 3: Dynamic Characteristics of Investigated Alloys.

#### Finite Element Model:

A numerical two-dimensional thermomechanical FE model was constructed to measure the plastic behavior of the alloys at various temperatures. A strip of the alloys is being pressed by a press over a die, as shown in Figure 10. The strip is 100 mm long, 1 mm thick, and held in place by a pressure pad. The press, pressure pad, and die all have 5 mm

fillets around the edges. The mechanical properties from Figure 5 for both A242 and A242 + TiB alloys were used in the FE simulation. The FE simulation was run multiple times while having the strip preheated to different temperatures. The temperatures used were RT, 50, 100, 150, 200, and 250°C. The strip was modeled using 2,500 two-dimensional quadratic plain strain elements with a total of 8511 nodes. Figure 11 shows a close-up of the developed FE mesh of the strip. For the boundary conditions, the strip was prevented from moving along the horizontal  $x$ -direction along surfaces a-b. The press, pressure pad, and die were all treated as rigid bodies with reference points  $RP_1$ ,  $RP_2$ , and  $RP_3$  for the boundary conditions. The press was prevented from movement and rotation in all directions at  $RP_1$  except the vertical  $y$ -direction, where it was forced to move 30 mm downward.

Similarly, the pressure pad was prevented from movement and rotation in all directions at  $RP_2$  except the vertical  $y$ -direction, where it was subjected to a force of value 440 kN acting downwards. As for the die, it was completely fixed in place at  $RP_3$ . A contact interaction was defined between the die and the strip's bottom surface with a coefficient of friction of 0.3. A similar interaction was



defined for the strip's top surface and the pressure pad. As for the contact between the press and the strip's top surface, frictionless contact was used.

## Results and discussion

### Simulation process

Figure 12 shows the deformed shape of the strip from the FE simulation. A close-up view of the developed stresses on the strip after the forming process using both A242 and the modified A242 + TiB alloys at 250 °C is shown in Figure 13. Figures 13A shows the stresses developed on the top half of the A242 strip, while Figures 13B shows them on the bottom half of the alloy. Similarly, Figure 13C, D shows the developed stresses for the top and bottom halves of the A242 + TiB strip. Figures 14, 15 show the developed stresses at the contact region between the strip and other rigid bodies for both alloys when the press moves by 5, 10, and 15 mm, respectively. To have an overall view of the stresses developed on both A242 and A242 + TiB alloys, Figure 16 shows the stresses developed on the strip's top and bottom surfaces at different locations for both alloys at room temperature (RT) and 250°C. At location A, the stresses are at their lowest points on the top surface but higher on the strip's bottom surface. The

temperature difference barely shows any effect on that location on both sides. At location B, the stresses on the top surface of the strip are still lower than on the bottom surface, but the effect of the temperature difference is visible. When at room temperature, the required stresses to deform both alloys are higher than at 250°C, which is expected due to the higher ductility of the material and strain softening at higher temperatures. At location C, the stress values reach their highest values. Furthermore, the stresses on both surfaces allow the top and bottom surfaces to be almost identical at higher temperatures. But, at room temperature, the top surface exhibits higher stresses due to the friction between the die and the strip's bottom surface. This causes the top surface to strain more than the bottom surface of the strip. At location D, the stress values drop when the strip is relieved from the bending stresses present at location E as it slides over the die. The stress values at location F are very small since the strip is sliding over the frictionless surfaces of the die and pressure pad.

Further simulations were conducted at various temperatures for both alloys to determine the stress variations at temperatures between RT and 250°C. Figures 17A, B shows the developed stresses for A242 at these temperatures, while Figures 17C, D shows the developed stresses for A242 + TiB. As expected, the increase in temperature causes a reduction in stresses due to the

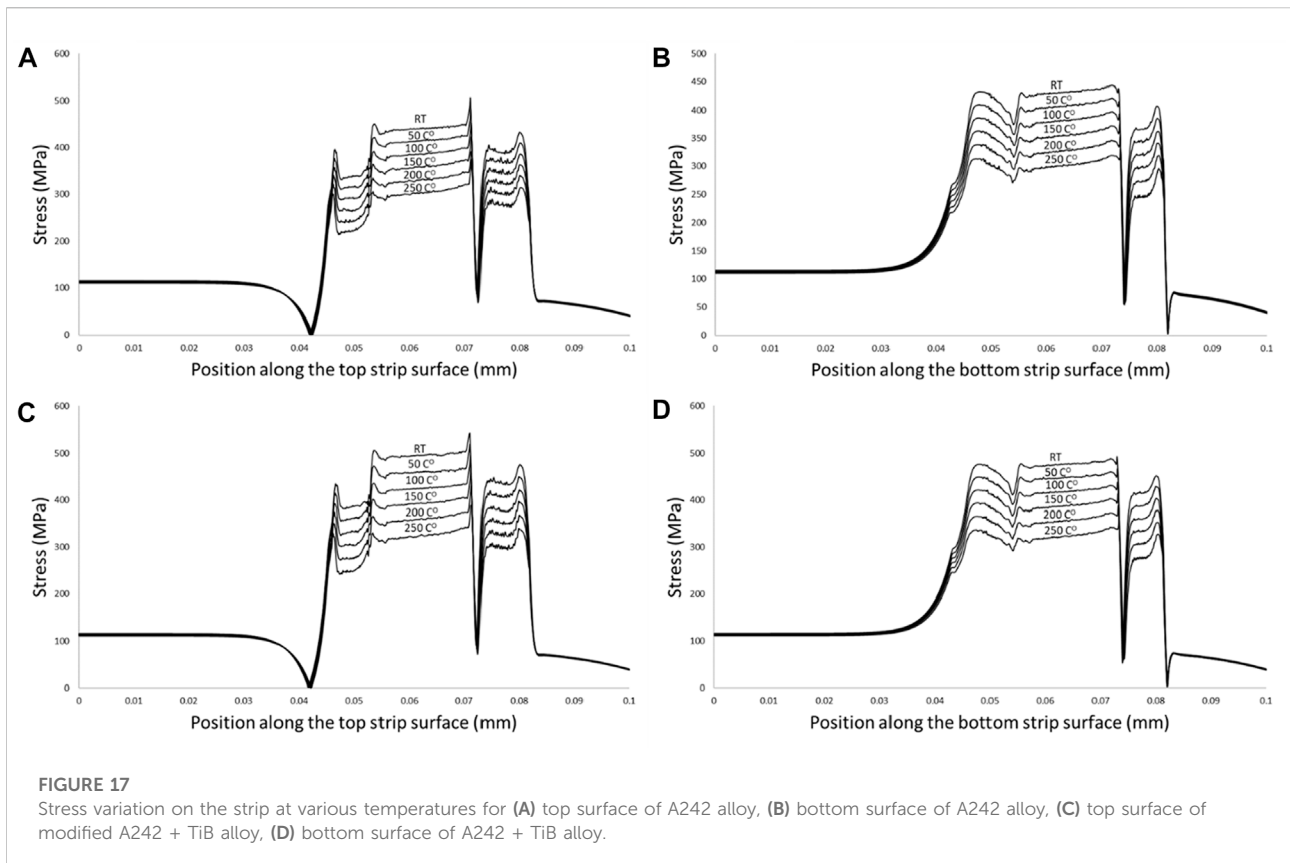


**FIGURE 17**

Stress variation on the strip at various temperatures for (A) top surface of A242 alloy, (B) bottom surface of A242 alloy, (C) top surface of modified A242 + TiB alloy, (D) bottom surface of A242 + TiB alloy.

reduced ductility of the materials. In all figures, the stresses at locations A, D, and F are almost unaffected by the increase in temperature. While locations B, C, and E are where the effect of raising the temperature is more prominent, This shows that the alloy A242 + TiB is more resistant to deformation than A242, even at high temperatures, making it suitable for highly elevated applications. At room temperature, the A242 + TiB alloy was more resistant to deformation than A242 by 9.1%. At 250 C, A242 + TiB was 7.6% more resistant.

## Conclusion

In the current investigation, A242 as-cast alloy is refined using TiB modifiers; thus, grain refinement plays an important role in the effect of the mechanical properties and the deformation process. From the microstructure observation, it is noticed that the grain size of the modified A242 + TiB alloy is reduced from 470  $\mu\text{m}$  to 35  $\mu\text{m}$ ; this is a significant enhancement in the microstructure refinement. Mechanical properties improved when deformation occurred at room temperature; for example, the modified A242 + TiB alloy rose 70 MPa more than the as-cast alloy. The dynamic properties showed an improvement in damping capacity

due to grain refinement, but the other dynamic properties did not significantly improve; this can be attributed to the elastic modulus, hardness, and density of the modified alloy and the as-cast alloy, which did not increase significantly. In the FRF diagram, the standard alloy A242 exhibited a higher resonant frequency than the modified alloy A242 + TiB, which can be attributed to the inhomogeneity of the as-cast alloy. On the other hand, the modified alloy shows fewer resonance peaks along the frequency range; this behavior results from the grain refinement and the good distribution of the intermetallic phases within the modified alloy. Furthermore, an FE simulation was conducted using both alloys to evaluate the plastic behavior of both alloys at various temperatures. The FE results have shown an improvement of A242 + TiB over A242, with 9.1% at room temperature and 7.6% at 250°C, which agrees with the experimental results of the improved mechanical properties of A242 + TiB alloy.

## Data availability statement

The data analyzed in this study is subject to the following licenses/restrictions: new patent will be submit. Requests to access these datasets should be directed to from our especial issue.



- process of the modified AlZnMgCu with 4%Si alloys. *Mater. (Basel)* 14 (20), 6154. doi:10.3390/ma14206154
- Moustafa, E. B., and Almitani, K. H. (2021). Detecting damage in carbon fibre composites using numerical analysis and vibration measurements. *Lat. Am. J. Solids Struct.* 18 (3). doi:10.1590/1679-78256294
- Moustafa, E. B. (2018). Dynamic characteristics study for surface composite of AMMNCs matrix fabricated by friction stir process. *Materials* 11 (7), 1240. doi:10.3390/ma11071240
- Moustafa, E. B., and Mosleh, A. O. (2020). Effect of (Ti-B) modifier elements and FSP on 5052 aluminum alloy. *J. Alloys Compd.* 823, 153745. doi:10.1016/j.jallcom.2020.153745
- Murty, B. S., Kori, S. A., and Chakraborty, M. (2002). Grain refinement of aluminium and its alloys by heterogeneous nucleation and alloying. *Int. Mater. Rev.* 47 (1), 3–29. doi:10.1179/095066001225001049
- Nafisi, S., and Ghomashchi, R. (2007). Boron-based refiners: Advantages in semi-solid-metal casting of Al-Si alloys. *Mater. Sci. Eng. A* 452–453, 437–444. doi:10.1016/j.msea.2006.10.146
- Nie, J. F., Shin, K. S., and Zeng, Z. R. (2020). Microstructure, deformation, and property of wrought magnesium alloys. *Metall. Mat. Trans. A* 51 (12), 6045–6109. doi:10.1007/s11661-020-05974-z
- Pattnaik, A. B., Das, S., Jha, B. B., and Prasanth, N. (2015). Effect of Al-5Ti-1B grain refiner on the microstructure, mechanical properties and acoustic emission characteristics of Al5052 aluminium alloy. *J. Mater. Res. Technol.* 4 (2), 171–179. doi:10.1016/j.jmrt.2014.10.017
- Reddy, N. S., Rao, A. P., Chakraborty, M., and Murty, B. (2005). Prediction of grain size of Al-7Si Alloy by neural networks. *Mater. Sci. Eng. A* 391 (1), 131–140. doi:10.1016/j.msea.2004.08.042
- Ren, L., Gu, H., Wang, W., Wang, S., Li, C., Wang, Z., et al. (2021). Effect of Sc content on the microstructure and properties of Al-Mg-Sc alloys deposited by wire arc additive manufacturing. *Metall. Mat. Int.* 27 (1), 68–77. doi:10.1007/s12540-020-00763-0
- Rodríguez, S. H., Goytia Reyes, R. E., Dwivedi, D. K., Gonzalez, O. A., and Baltazar Hernandez, V. H. (2012). The effect of Al-5Ti-1B on microstructure and mechanical properties of Al-12Si-xFe alloy. *Mater. Manuf. Process.* 27 (6), 599–604. doi:10.1080/10426914.2011.560230
- Sigworth, G. K., and Kuhn, T. A. (2007). Grain refinement of aluminum casting alloys. *Inter. Met.* 1 (1), 31–40. doi:10.1007/bf03355416
- Suwanpreecha, C., Pandee, P., Patakham, U., and Limmaneevichitr, C. (2018). New generation of eutectic Al-Ni casting alloys for elevated temperature services. *Mater. Sci. Eng. A* 709, 46–54. doi:10.1016/j.msea.2017.10.034
- Trejo Rivera, N. M., Torres Torres, J., and Flores, A. (2019). Valdés A-242 aluminium alloy foams Manufacture from the Recycling of beverage cans. *Metals* 9, 92. doi:10.3390/met9010092
- Wang, B. B., Xie, G., Wu, L., Xue, P., Ni, D., Xiao, B., et al. (2021). Grain size effect on tensile deformation behaviors of pure aluminum. *Mater. Sci. Eng. A* 820, 141504. doi:10.1016/j.msea.2021.141504
- Wang, E. R., Hui, X., Wang, S., Zhao, Y., and Chen, G. (2010). Improved mechanical properties in cast Al-Si alloys by combined alloying of Fe and Cu. *Mater. Sci. Eng. A* 527 (29), 7878–7884. doi:10.1016/j.msea.2010.08.058
- Wang, F., Qiu, D., Liu, Z. L., Taylor, J., Easton, M., and Zhang, M. x. (2014). Crystallographic study of Al3Zr and Al3Nb as grain refiners for Al alloys. *Trans. Nonferrous Metals Soc. China* 24 (7), 2034–2040. doi:10.1016/s1003-6326(14)63309-4
- Wu, X.-F., Wang, K. Y., Wu, F. F., Zhao, R. D., Chen, M. H., Xiang, J., et al. (2019). Simultaneous grain refinement and eutectic Mg2Si modification in hypoeutectic Al-11Mg2Si alloys by Sc addition. *J. Alloys Compd.* 791, 402–410. doi:10.1016/j.jallcom.2019.03.326
- Zecevic, M., Lebensohn, R. A., McCabe, R. J., and Knezevic, M. (2019). Modelling recrystallization textures driven by intragranular fluctuations implemented in the viscoplastic self-consistent formulation. *Acta Mater.* 164, 530–546. doi:10.1016/j.actamat.2018.11.002
- Zhu, J., Jiang, W., Li, G., Guan, F., Yu, Y., and Fan, Z. (2020). Microstructure and mechanical properties of SiCnp/Al6082 aluminum matrix composites prepared by squeeze casting combined with stir casting. *J. Mater. Process. Technol.* 283, 116699. doi:10.1016/j.jmatprotec.2020.116699